Journal of
Applied Remote Sensing

Spectral mapping of the Paraíba do Sul River plume (Brazil) using multitemporal Landsat images

Natália de Moraes Rudorff
Milton Kampel
Carlos Eduardo de Rezende

SPIE

Spectral mapping of the Paraíba do Sul River plume (Brazil) using multitemporal Landsat images

Natália de Moraes Rudorff,[a] Milton Kampel,[a] and Carlos Eduardo de Rezende[b]

[a] Instituto Nacional de Pesquisas Espaciais, Divisão de Sensoriamento Remoto, Av. dos Astronautas, 1758, 12227-010, Jd. da Granja, São José dos Campos, SP, Brazil
nmr@dsr.inpe.br, milton@dsr.inpe.br

[b] Universidade Estadual do Norte Fluminense, Centro de Biociências e Biotecnologia, 2813-600, Campos dos Goytacazes, RJ, Brazil
crezende@uenf.br

Abstract. Coastal zones are influenced by oceanic, atmospheric, and continental forces, which make them highly vulnerable to climate and anthropogenic changes. The Paraíba do Sul River (PSR) Estuary (Brazil), is especially affected by intensive industrial, urban, and rural activities, along its catchment area. Few works, though, have been done concerning the impacts of these changes. Remote sensing is, thus, an important and unique tool to assess the past scenes for a temporal analysis. The present work aimed to analyze spatial-temporal trends of the PSR plume from 1985 to 2009, using Landsat 5 TM images. Two spectral classification methods were used to map the river plume: maximum likelihood and spectral linear mixture analysis (SLMA). The images corresponded to the months of greatest river discharge, totalizing 11 cloud-free images. Geographical, radiometric, and atmospheric corrections were applied to the five spectral bands used for the classification. Both methods showed good results, however the SLMA provided more information of the water constituent's distribution. The sediment river plume and inner shelf phytoplankton dominated waters showed a negative trend associated with a diminishing of the river discharge. Further works concern *in situ* validation of the classifications, bio-optical modeling, and more investigations of climate and anthropogenic changes on the PSR.
 [DOI: 10.1117/1.3630220]

Keywords: image analysis; Landsat TM 5; spatial and temporal analysis; Paraíba do Sul River plume.

Paper 11053R received Mar. 25, 2011; revised manuscript received Jun. 13, 2011; accepted for publication Aug. 9, 2011; published online Sep. 6, 2011.

1 Introduction

Rivers are an important source of inorganic sediment, organic particles, and dissolved nutrients, transported into coastal areas by river runoff.[1] The balance of these elements has important effects to coastal processes and environmental health.[2] Despite their importance, rivers have suffered great pressure from human activities and land use changes.[3] Alterations in their regime and water quality can cause serious effects, such as eutrophication processes due to exceeded organic loads;[4] ecological disruptions with diminished outflow;[5] and erosion or accumulation, due to unbalanced sediment transport[6] (for more examples, see Ref. 2). The Paraíba do Sul River (PSR) is one of the main rivers of the most populated region of Brazil—the southeast.[7] It is a very important hydrologic resource, but has been suffering great pressure due to many anthropogenic activities along the catchment area, such as dam construction, industrial employment, urban areas with some untreated sewage effluents, agriculture activities, and sand exploitation. Marengo

1931-3195/2011/$25.00 © 2011 SPIE

and Alves[8] reported a significant decrease of the PSR discharge during the past decades, associated mainly with the land use impacts rather than climate change. Effects of changes in the hydrological regime and water quality of the PSR have been less studied in its estuary and coastal zone. Understand these processes and changes through time, are important to point out the main stressors and their impacts, in order to offer subsidies for management authorities to implement adaptive actions for sustainable use.[9,10]

Satellite imagery offers a synoptic view of the environment and is a very useful data source to study environmental and land use changes. Landsat 5 TM has provided images since 1985 and is still in operation, offering a long time series. The sensor has 30 m of nominal spatial resolution, which gives good details for medium scale areas, and 6 spectral bands located in the visible and infrared region that may be applied for mapping coastal and inland waters.[11–14]

Coastal areas, especially with the presence of river runoff, are characterized by complex waters due to the mixture of optically active substances (OAS), such as inorganic sediments, organic colored dissolved substances, and photosynthetic pigments.[15] To separate water types with the dominant constituents in these optically complex systems, is not a trivial task. Some spectral classification methods have been proposed to map waters in continental and coastal systems using satellite imagery. Thomas and Weatherbee[16] and Lihan et al. [17] proposed a classification method of the river plume and coastal waters based on the maximum likelihood (ML) method, with good results for a temporal analysis. The method is simple and based essentially on a visual inspection of each image to empirically collect reference training polygons for the water classes. This, though, may be a very subjective and laborious procedure, since every image has to be checked for new training polygons due to spatiotemporal spectral variations. Another method that may be applied to map river plumes and OAS in optically complex systems is based on the spectral linear mixture analysis (SLMA).[18–20] The SLMA requires the use of "pure" end-members as a spectral reference for each OAS, and maps the fractional abundance of the OAS present in the scene. The end-members may be obtained by selection techniques that are less subjective, and with the use of different images, to construct mean standard spectral references that can be afterwards applied to a series of images for a temporal analysis.[20,21] Nevertheless, this method also has some limitations, as variations in the quality of the water components are challenges to the end-member selection, and nonlinear spectral responses can induce errors in the analysis.

The present work aims to analyze the temporal evolution of the PSR plume and adjacent coastal waters, from 1985 to 2009, using Landsat 5 TM images with the application of two spectral mapping methods: the ML and SLMA. Advantages and limitations of each method are discussed and results of the mapped plume area are compared to *in situ* data of the river discharge.

2 Material and Methods

2.1 Site Location and Description

The PSR is located in the southeast of Brazil, passing through three states: São Paulo, Minas Gerais, and Rio de Janeiro, were it finally drains off into the Atlantic Ocean (21° 36′ S and 41° 05′ W) (Fig. 1). The catchment area is approximately 57,000 km^2 and the river has 1180 km of length, considered medium size.[7] The southeast is a very important economic region of Brazil, and along the PSR there are many human activities, such as urban habitations, industries, agriculture, sand exploitation, and hydroelectric reservoirs. All these contribute to different degrees of impacts to the PSR hydrologic regime and water quality.[8] The lowest river discharge is during the dry austral winter season (June to September) and can reach a minimal of 180 m^3 s^{-1} near the estuary mouth. The highest is during the rainy summer season (November to March), with a maximum of 4400 m^3 s^{-1} (Ref. 22).

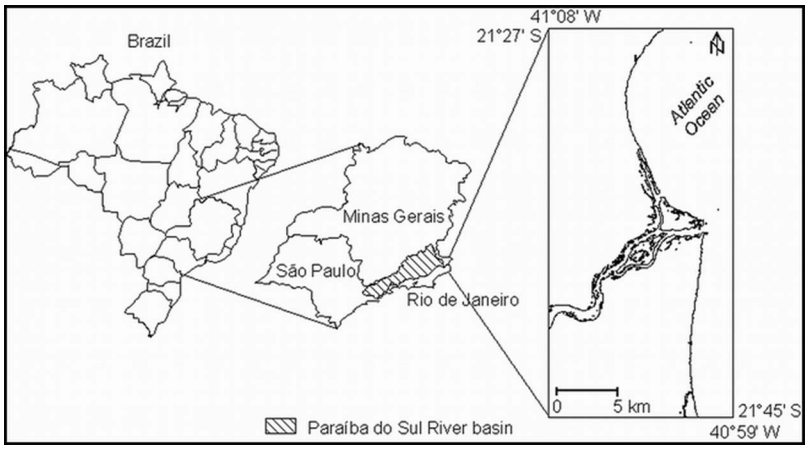

Fig. 1 Localization of the study area.

2.2 Satellite Data

Besides the long term availability of images, since 1984, the 30 m spatial resolution of Landsat TM images is also better applied for water quality analysis of medium size rivers.[11,12] Level 2 preprocessed images of the Landsat 5 TM, covering the PSR estuary and adjacent ocean, were obtained from the Brazilian's National Institute for Space Research (INPE) database. The five spectral bands of the visible and near-medium infrared were used for the analysis (Table 1). Initially, both dry and wet seasons were analyzed for each year; however, images acquired during the dry period did not show a well formed plume of the river. This way, only one image representing the month with the greatest river discharge of each year was chosen (January, February, or March). Images were selected based on discharge tables and cloud-free criteria. In total, 11 images were used: 02/1985, 02/1986, 02/1991, 01/1994, 01/1997, 01/1999, 03/2004, 02/2005, 03/2006, 02/2007, and 02/2009 (month/year).

2.3 Image Preprocessing

2.3.1 Registration

The images were registered using a georeferenced image base acquired from the GeoCover Landsat TM dataset. Eleven points of control were used for the registration and the nearest neighbor technique for interpolation. This method was chosen in order to preserve original digital values of the image. The highest root mean square error (RMSE) was of 0.37 pixel (of 30×30 m), using a second degree polynomial.

Table 1 Landsat-TM 5 band numbers and correspondent central wavelengths (Ref. 23).

Band number	wavelength (nm)
1	485
2	569
3	660
4	840
5	1676

2.3.2 Subset area

A subset area was selected in the scene embracing only the PSR estuary and coastal adjacent area: 21°9–21°50′ S and 40°43–41°10′ W.

2.3.3 Radiometric calibration

Each band was calibrated using rescaling factors, converting digital numbers to radiance, and afterwards to top-of-atmosphere (TOA) reflectance. Among the parameters used for the radiometric calibration were: minimum and maximum values of radiance, for each band, the sun elevation angle, and solar distance in astronomical units.[23] Theses conversions are important to standardize the data in the scene and in between bands.

2.3.4 Atmospheric correction

One of the most critical steps for water quality analysis is the atmospheric correction, since the water signals are very low and small errors may lead to high uncertainties in the water quality retrieval.[24] This is especially challenging in coastal areas because of the presence of complex continental aerosols and waters with suspended inorganic sediments (SIS) and high concentrations of chlorophyll.[25–27] These last ones may have reflectance signals in the infrared bands, which are mostly used by correction algorithms as null baselines for water reflectance. The black pixel assumption, widely used for atmospheric correction, assumes that the water highly absorbs in the infrared, and scattering contribution should be only from atmospheric aerosols. This, though, may not be true for waters with SIS and high concentrations of chlorophyll, especially for the near-infrared (NIR) bands.[26,27] In the present work, the 6S radiative transfer model was used to correct the atmospheric interference and calculate the water's superficial reflectance.[28] Input data contained, besides the TOA reflectance, satellite, sensor and band information, and date, hour, and geographical information of the scene. The tropical atmospheric and marine aerosol models were used to fit environmental conditions of the area. The visibility parameter used to retrieve the aerosol optical thickness (AOT) was estimated using the darkest pixel assumption, with the B1 blue band,[29] and two infrared bands, in the NIR and short wave infrared (B4 and B5), through an iterative process. The first value assumed was 40 km of visibility (clear sky), which was readjusted until a threshold of 1% to 10% reflectance for B1,[29] and 0% for the NIR and SWIR, at the darkest offshore areas, was achieved. The use of the SWIR band to estimate the AOT was used to minimize the influence of the SIS and high chlorophyll in the reflectance of the water surface.[26,27]

2.3.5 Land-water and cloud mask

A mask was applied for the land, clouds, and shadow present in the scene in order to classify only the water body. Land and water were previously separated using the SWIR B5 band. Water has a very low reflectance in this spectral region, even in the presence of suspended material, in contrast to the land, which has mainly a high reflectance. In this manner, reflectance values lower than 10% were primarily classified as water. Afterwards a raster edition was made using a 543 (RGB) false color composition, considered to be good for land–water separation using Landsat TM.[30] Clouds were classified as a mask using a high reflectance threshold in all bands and a raster edition was made to incorporate the shadows in the mask. Stripes present in the Landsat TM images were not removed through filtering techniques, in order to preserve the original reflectance values.

Table 2 Number of training polygons and pixels (polygons/pixels) used for the ML classification for each water type, in all images.

Year	Plume core	Plume and inner shelf waters	Other inner shelf waters	Offshore water
1985	6 / 336	5 / 490	7 / 457	5 / 476
1986	2 / 163	3 / 181	2 / 180	3 / 658
1991	3 / 164	4 / 440	3 / 283	3 / 856
1994	3 / 150	4 / 286	5 / 572	4 / 981
1997	3 / 301	9 / 1168	5 / 621	3 / 526
1999	3 / 230	5 / 306	4 / 333	3 / 502
2004	2 / 191	5 / 526	7 / 937	3 / 1228
2005	2 / 261	3 / 631	5 / 979	5 / 740
2006	2 / 278	6 / 392	4 / 331	5 / 560
2007	2 / 212	7 / 423	5 / 412	5 / 457
2009	3 / 225	4 / 218	5 / 423	4 / 535

2.4 Spectral Mapping and Classification

2.4.1 ML

The ML (Ref. 31) is a statistical classifier that uses resemblance of statistical properties, such as mean and variance, to calculate the probability of an element to be part of a class. This classification is called supervised because there is a direct interaction with the one who chooses the training pixels or polygons as a spectral reference to represent each class. Based on the spectral statistical properties of the chosen reference, the pixels of the scene will be grouped in the classes. The result is a classified image and rule images of each class.

The first procedure for the ML method is to define the classes intended to be separated, and select the training pixels or polygons in each image. The water classes used in this work were defined according to Thomas and Weatherbee,[16] Lihan et al.,[17] and after a visual inspection of the scenes. The classes were: 1. Plume core: located immediately off the river mouth, with the highest reflectance values, especially in the longer wavelengths; 2. Plume and inner shelf waters: mixed waters at the plume boundaries, with intermediate reflectance values; 3. Other inner shelf waters: characterized by coastal waters far from the river mouth, with high reflectance values in shorter wavelengths; and 4. Offshore waters: characterized by clear ocean waters at the offshore areas, with low reflectance values at all wavelengths.[16,17] The training polygons were selected on the areas directly influenced by these four water types using a true color image composite (321), and analyzing the spectral signals of each water type. The number of training polygons used for each class in each image is given in Table 2. They varied according to the size of the classes and their spectral variability (e.g., the plume and inner shelf waters class had a high spectral variability, so more training polygons were necessary to represent this class).

Classifications were evaluated according to the spectral separability between classes, based on Jeffries–Matsushita distance,[17] and a validation scheme based on a visual interpretation of the scene, since there were no available ground truth data. Independent validation polygons, with a regular distribution, were systematically collected in each scene, and classified according to the visual interpretation with a true color composite (321). Afterwards, a stratified random sampling of pixels in each polygon was collected for the validation of the ML classifications, with the confusion matrix. The percentage of accuracy and kappa coefficient were used to analyze the performance of each classification.[32]

2.4.2 SLMA

The SLMA (Ref. 33) is a spectral mapping method in which the main objective is to determine the fractional abundance of the elements present in the scene. These elements are represented

by end-members that have unique spectral properties. The basic concept is that each pixel in the scene is a linear mixture combination of the elements, which results in a specific spectral response, according to the fractional abundance of each end-member. The algorithm can be expressed by the following formula:

$$R_{\mathrm{pi}} = \sum f_{\mathrm{j}}\, r_{\mathrm{ij}} + \varepsilon_{\mathrm{i}}. \tag{1}$$

Where R_{pi} is the water remote sensing reflectance at a pixel p and band i; f_j is the fractional abundance of the j'th end-member; r_{ij} is the reflectance of the j'th end-member in the i'th band, and ϵ is the calculated error. The sum of the fractions at each pixel must be 1, or at least close to. The results are images of the mapped fractional abundance of each element present in the scene.

The critical part of the SLMA is to collect end-members that represent pure elements present in the scene. This is especially difficult for optically complex waters that have different OAS simultaneously mixed in the water column.[19] Two methods for extracting end-members were tested. The first was visually selecting pixels in the scene that represent each water type, and using the mean spectra as the end-member. The second was using the minimum noise fraction (MNF) transformation, which is a spectral data reduction technique[34] similar to a principal components analysis. Each new band gathers one type of information based on the variance of the reflectance values. The original bands are highly correlated, so it is more difficult to separate information based on each band. The MNF technique may therefore allow to better separate the information and choose more pure pixels related to each component.[34] The first band separated the river plume, the second inner shelf waters, the third offshore clear ocean waters, and the fourth and fifth wore only noise. The bands were visualized in an n-dimensional visualizer attribute space,[35] where the end-members associated with the water types were collected. Their reflectance spectra were also examined to confirm the water type identification. The second method had better results than the first, with less RMSE and fraction values closer to the 0 to 1 interval. Fraction values out of this range may be caused by less pure end-members.[20] Hence, the second method was chosen to follow the classification analysis.

Images of different dates were used for the end-member selection in order to gather more spectral information due to the temporal variability of water components.[20] This procedure allowed the construction of a spectral library with a mean standard spectrum for each end-member that could, afterwards, be applied for all images.

The end-members were representative of: 1. River sediment plume; 2. Other inner shelf waters; and 3. Offshore waters. The plume and inner shelf waters mixed zone was not chosen as an end-member because the SMLA supposes end-members as "purely spectrally unique" and each pixel is already a mixture of the elements. The SLMA was applied using the same spectral library for all images to map the fractional abundance of each water type. The results were evaluated with the fractional interval and RMSE.

2.4.3 Classification comparison

In order to compare the methods, the SLMA results were converted into classification maps, with classes separated by intervals of the fractional abundance of each water type: 1. high abundance: 0.66 to 1.00; 2. medium abundance: 0.33 to 0.66; and 3. lower abundance: 0.10 to 0.33. The SLMA and ML classes were visually compared and advantages and limitations of each method were discussed.

2.5 Temporal Analysis

Temporal analyses were done comparing the classified area of the river sediment plume and inner shelf waters, with the PSR discharge. Areas with the presence of clouds were grouped in

Table 3 Estimated visibility and correspondent AOT using the 6S model and the darkest pixel assumption, for each image.

Year	Visibility (km)	AOT
1985	10	0.43
1986	8	0.52
1991	12	0.37
1994	5	0.78
1997	20	0.26
1999	10	0.43
2004	20	0.26
2005	12	0.37
2006	10	0.43
2007	10	0.43
2009	23	0.23

the surrounding classes in order to estimate the total area of each class. The river discharge was obtained from ANA–National Water Agency monitoring program, at a station located near the PSR estuary (Campos, RJ −21° 45′ S 41°18′ W) and at the same dates of the acquired images. Spearman correlation analyses were made to evaluate the dependence in between the classes and the river discharge. Linear regression analysis was used to detect temporal trends of the classes and river discharge, and associate with possible changes in the PSR hydrological regime and water quality.

3 Results and Discussion

3.1 Spectral Mapping and Classifications

The visibility estimated for the atmospheric correction ranged from 23 km (clear sky) to 5 km (hazy), corresponding to 0.23 to 0.78 AOT (Table 3).

The mean and standard deviation reflectance values of the ML classes for all images, and the SMLA end-members, without and with the radiometric and atmospheric correction are given in Fig. 2 and Tables 4 and 5.

The mean reflectance of the raw digital numbers (DNs), without radiometric and atmospheric correction [Figs. 2(a) and 2(c)], had higher values especially in the shorter wavelengths, and much higher standard deviations among the classes. The higher values in the blue spectral region are caused by the Rayleigh scattering of the atmospheric molecules, which has an exponential increase toward shorter wavelengths. This spectral region is the most affected by the atmosphere; notwithstanding, it is also the most important region for the retrieval of the water components. Phytoplankton and dissolved and particulate organic matter have their highest absorption features in the blue and ultraviolet spectral region.[15] This is mainly why the radiometric and atmospheric corrections are a crucial step for water quality analysis of remote sensing data.[25] Besides that, the water reflectance is very low and slight variations on the spectra, caused by sensor radiometric limitations and atmospheric interference, may lead to high errors in the estimation of the water components and classification of water types.[24] A great challenge of the atmospheric correction of coastal areas is the presence of SIS that limits the use of the black pixel assumption to estimate the AOT especially with the NIR bands. In the present work, the combined use of the NIR and SWIR bands to estimate the AOT minimized the effect of the SIS reflectance. In most images the sediment river plume still showed considerably high values of reflectance in the NIR band, while at the SWIR B5 band the reflectance values of the water, over the entire scene, were lower and more homogeneous. No negative values were retrieved for the blue bands which indicate that there were no overestimations of AOT due to the SIS influence.[27] The radiometric and atmospheric corrections presented more realistic spectral signatures of the water types, with better defined spectra [Figs. 2(b) and 2(d)] and lower SD (Tables 4 and 5). This step was

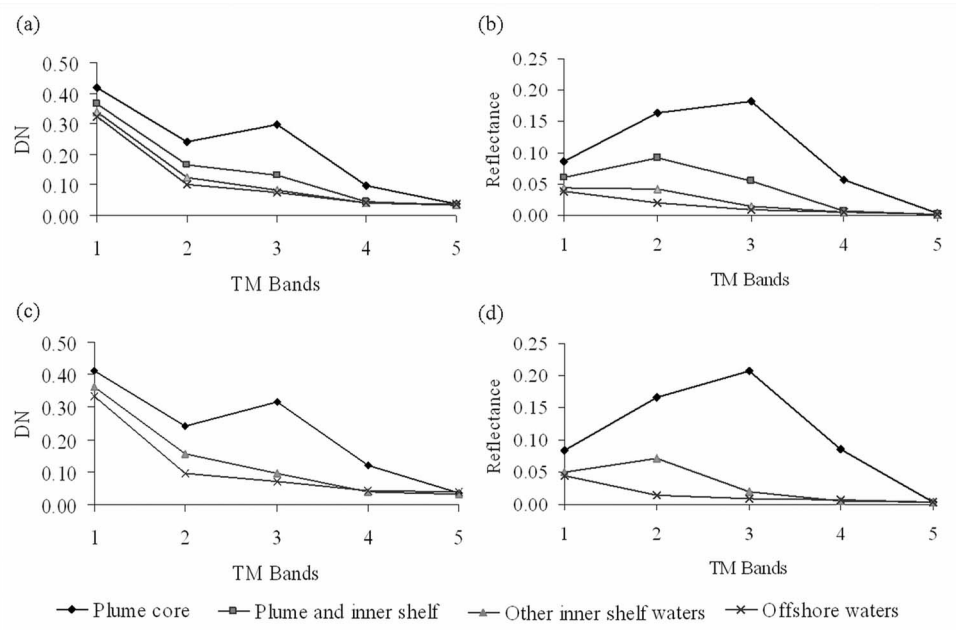

Fig. 2 Mean spectra of the raw DNs (a) and reflectance values with radiometric and atmospheric corrections (b), of ML classes for all the images; and mean spectra of the raw DNs (c) and reflectance values with radiometric and atmospheric corrections (d) of the SMLA end-members, for all images.

essential for the multitemporal image analysis and the application of the same end-members for all images in the SMLA.

There were some small variations of the mean reflectance spectra of the ML training polygons among the images, mainly on the magnitude rather than the shape of the spectra. Magnitude oscillations may be caused by different concentrations of the OAS, while spectral slope variations

Table 4 Standard deviation of all classes in all images, for the ML classification, using the raw DNs and the reflectance values with radiometric and atmospheric corrections.

Raw DNs								
	Plume core		**Plume and inner shelf waters**		**Other inner shelf waters**		**Offshore waters**	
TM Bands	**min**	**max**	**min**	**max**	**min**	**max**	**min**	**max**
1	0.005	0.014	0.004	0.014	0.003	0.025	0.003	0.010
2	0.008	0.023	0.005	0.031	0.005	0.195	0.002	0.020
3	0.012	0.025	0.003	0.341	0.004	0.018	0.002	0.020
4	0.007	0.025	0.003	0.019	0.003	0.008	0.003	0.007
5	0.003	0.011	0.003	0.007	0.002	0.006	0.002	0.006
Reflectance with radiometric and atmospheric correction								
	Plume core		Plume and inner shelf waters		Other inner shelf waters		Offshore waters	
TM Bands	min	max	min	max	min	max	min	max
1	0.001	0.003	0.001	0.002	0.000	0.002	0.000	0.001
2	0.001	0.003	0.001	0.004	0.001	0.003	0.000	0.002
3	0.002	0.004	0.001	0.005	0.000	0.002	0.000	0.002
4	0.001	0.003	0.000	0.002	0.000	0.001	0.000	0.001
5	0.000	0.001	0.000	0.001	0.000	0.001	0.000	0.001

Table 5 Standard deviation of the SMLA end-members, collected from all images, for the raw DNs, and reflectance values with the radiometric and atmospheric corrections.

	Raw DNs				Reflectance with radiometric and atmospheric corrections			
TM bands	Plume core	Plume and inner shelf waters	Inner shelf waters	Offshore waters	Plume core	Plume and inner shelf waters	Inner shelf waters	Offshore waters
1	0.050	0.070	0.035	0.012	0.022	0.017	0.026	0.011
2	0.031	0.037	0.013	0.010	0.029	0.021	0.026	0.007
3	0.040	0.026	0.014	0.009	0.029	0.018	0.014	0.004
4	0.022	0.010	0.011	0.009	0.021	0.006	0.004	0.004
5	0.012	0.015	0.016	0.009	0.003	0.004	0.004	0.005

are more associated to quality differences of the water components.[15] However, the main source of spectral variations in between the scenes was due to the spatial distribution of the water types. Almost on every image the training polygons had to be relocated to adjust to the new distribution. Spatial and temporal variations of the water reflectance in coastal areas can be caused by a number of factors including storms, seasonal cycles, magnitude and direction of wind stress, currents, bathymetry, discharge strength, and dispersion angle of river plumes, among others.[36] These stretchers cause several internal and external processes which are responsible to induce, in terms of quality and quantity, large variations of OAS in the water surface. Nevertheless, in the present study, all images were from the same season, presenting similar dominant oceanographic and meteorological conditions. Thus, even with relatively high spatial variations, the spectral variations of the water types were not very meaningful, allowing the application of a single mean spectral reference for each end-member on the SLMA.

The ML classes had similar mean spectra as the SLMA end-members [Figs. 2(b) and 2(d)]. The SLMA end-members had slightly more extreme values, because they should represent "pure pixels" of each class. The river plume had a reflectance spectrum likely characterized by the dominance of SIS. There is an increasing reflectance from the blue (B1) to the red (B3) band, and still a considerable high reflectance at the NIR band (B4). The reflectance is generally very low in the infrared, due to high water absorption in this spectral range. However, in the presence of high concentrations of inorganic sediments, the reflectance signal can be higher in the NIR and even SWIR bands.[15,37,38] The "other inner shelf waters" class was likely characterized by the dominance of phytoplankton, with higher reflectance in the green band (B2), and lower in the chlorophyll *a* absorption bands (B1 and B3). The "plume and inner shelf waters" class was likely characterized by a mixture of the sediment plume and phytoplankton dominated coastal waters, with higher reflectance in the green, and secondary in the red band. "Offshore waters" was likely characterized by clear ocean waters with low reflectance values over all the spectra, because of the low concentrations of OAS. The blue band (B1) has a slightly higher reflectance due to the Rayleigh scattering of the water molecules.[15] Similar spectral curves characterizing these water types in coastal areas were also found by Froidefond et al.[39] and Lihan et al.[17]

All classes had high degrees of separability in the ML classification, following the Jeffries–Matsushita distance, with values from 1.96 to 2.0 (maximum). The classes that were least separated were offshore waters and other inner shelf waters, followed by other inner shelf waters and plume and inner shelf waters. The best separation was between "sediment plume core" and offshore waters. In the validation analysis all ML classifications had a very good overall accuracy and kappa coefficient, ranging from 0.79 for the 2004 classified image, to 0.94 for 1997 (Table 6). The highest confusion was in between the plume and inner shelf waters mixed zone and the other inner shelf waters. Indeed, some areas that were far from the river influence had very similar spectral responses as the plume mixed zone. This may be because of the presence of other small rivers and sand resuspension at the surf zone areas along the coast.

Table 6 Number of training polygons and pixels (polygons/pixels) of each class used for the validation of the ML classification, and the overall accuracy and kappa coefficient, for every image.

Year	Plume core	Plume and inner shelf waters	Other inner shelf waters	Offshore water	Overall accuracy	Kappa coefficient
1985	4 / 296	11 / 545	11 / 1,791	7 / 3,798	94.9%	0.93
1986	3 / 535	4 / 703	9 / 1,553	12 / 1,825	91.5%	0.88
1991	2 / 319	6 / 870	4 / 634	13 / 1,878	86.7%	0.80
1994	2 / 341	8 / 1,320	14 / 2,047	11 / 1,536	93.8%	0.91
1997	5 / 848	11 / 1,773	5 / 790	9 / 1,313	95.4%	0.94
1999	3 / 514	10 / 1,103	9 / 846	17 / 2,294	76.7%	0.64
2004	2 / 224	7 / 1,176	19 / 2,934	8 / 1,167	86.8%	0.79
2005	4 / 535	12 / 2,218	8 / 1,291	13 / 2,022	94.1%	0.92
2006	2 / 3,511	11 / 18,335	8 / 13,703	10 / 16,320	86.9%	0.81
2007	4 / 7,607	13 / 24,131	11 / 31,472	7 / 20,010	87.9%	0.83
2009	4 / 6,218	10 / 16,669	11 / 18,764	12 / 18,802	89.7%	0.86

The SLMA in general showed a good coherency with the ML classifications. The mapped fractions had some negative and over 1 values, but generally all water types showed a reasonable fit. The "sediment plume" fraction had the closest values to the 0 to 1 interval, and the other inner shelf waters had the worst fit. The minimum and maximum values of the fractions, for all images, ranged from: −0.12 to 1.40 for the sediment plume; −1.61 to 2.20 for other inner shelf waters; and −1.22 to 2.49 for offshore waters. Values representative of less than 10 pixels where not considered in the analysis, since they were found to be from spurious pixels and not representative of the overall result. Fractions out of the 0 to 1 range mean that the algorithm overestimated some elements, while underestimated others. These errors may happen when the selected end-members are not really representative of pure elements. Indeed the worst fit was for the other inner shelf waters, which has the highest mixture of OAS. The difficulty in extracting pure elements from an image scene of optically complex waters is discussed by Novo and Shimabukuro.[18] The water components do not occur isolated in the environment and there is always a mixture of them in the water column. The course spatial resolution of the area sampled by the orbital sensor also contributes to a greater mixture of the OAS in each pixel. Besides the difficulties in separating pure elements in the scene, the low water reflectance, especially when there are low concentrations of OAS, make their classification even more difficult. Small variations in the water constituents and contributions from external sources such as the atmosphere, water surface agitation, presence of bubbles, and whitecaps, can introduce errors that are especially significant in areas with very low reflectance values.[40] This is probably why the offshore waters also had higher uncertainties compared to the sediment plume, despite being the water type which should have the least mixture of OAS.

The fractional abundance of each end-member had a coherency distribution with the water types in the scene. The sediment plume fraction (f_{plume}) [Fig. 3(a)] had higher values at the river mouth, and delineated well the plume core and dispersion zone. The inner shelf water fraction (f_{inner}) [Fig. 3(b)], dominated by phytoplankton, had higher values closer to the coast and decreasing toward the open ocean. High values of this fraction were also encountered at the plume dispersion zone, demonstrating also a high contribution of the phytoplankton in the area influenced by the river plume. The offshore fraction (f_{offshore}) [Fig. 3(c)] of ocean clear waters was higher over the offshore area, as expected.

The RMSE gives information of the accuracy of the model by the rms difference of the model estimated reflectance with the "true" reflectance values of each pixel. The highest RMSE of all images was of 0.041, with the greatest uncertainties associated with the mixed zone of the plume dispersion and inner shelf waters [Fig. 3(d)]. The mixed zone is truly the most difficult to model, with the highest mixture of the OAS. Besides the complex of the mixture, waters with high SIS concentration tend to have higher uncertainty in its estimation due to the spectral

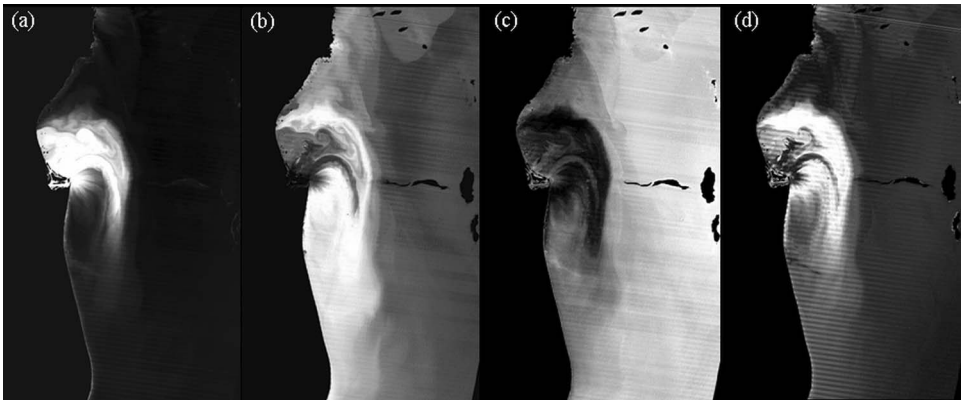

Fig. 3 Mapped fraction abundance of the end-members by the SMLA, on the 1985 image: f_{plume} (a); f_{inner} (b); $f_{offshore}$ (c); RMSE (d). Brightness corresponds to higher values (each band with different ranges close to 0 to 1).

dominance of the SIS over the other OAS. The high reflectance of the SIS is very good for its own retrieval, however masks the presence of the other OAS, with lower spectral signatures.[20,21]

Visually comparing the true color composite (321) with the classification results, both methods seemed to map well the water types. However, some differences can be observed between the classifications (Figs. 4–6). In general, the advantages of the ML classification were that, since every image had to be carefully inspected, in some cases the plume dispersion area was noticeably composed not only of dominated SIS waters, but also of phytoplankton dominated waters, with a very dark greenish color. In these cases this water type was grouped in the plume and inner shelf waters mixed class, as it was clearly part of the plume dispersion. While, in the SMLA, since each constituent is mapped separately, it was not possible to group different constituents in the same class to characterize a specific phenomenon. On the other hand, the SMLA allowed to map the fractional abundance of each constituent, which gave more information of their distribution in the scene. Besides this, with the SMLA result, it is possible to analyze the spectral variability of the scene, associated with the quality and quantity of the OAS. This information is not given by the ML method.[16,17]

However, there were also some limitations in the SLMA classification. High values of the coastal water fraction were found in the sediment plume area because of the misbalanced factional abundance. This may have been caused by nonlinear spectral behavior between the OAS, due especially to the spectral dominance of the SIS and the use of non pure end-members.[21] The presence of haze may also introduce some overestimation of phytoplankton dominated waters.[21] This was observed in some images were some offshore areas near the presence of clouds were classified as low abundant inner shelf waters [e.g., Figs. 4(c) and 4(k)].

In general, both the ML and SLMA showed a coherency mapping between the classifications and in comparison to the true-color composite image. Further investigations may be performed to compare the results with ground truth data, also to confirm the reliability and accuracy of the classifications. Each classification method has its own advantages and limitations. For a multitemporal approach, the SLMA method however seemed to offer a better analysis tool of the spectral variability among the scenes, besides being a more practical and less subjective technique for the application on a long time series. Nevertheless, the results should be analyzed with care as some uncertainties have also been pointed out.

3.2 Temporal Analysis

The monthly mean river discharge of the PSR estuary from 1985 to 2008 is shown in Fig. 7. There is a clear seasonal cycle of the river discharge marked by dry austral winter and rainy

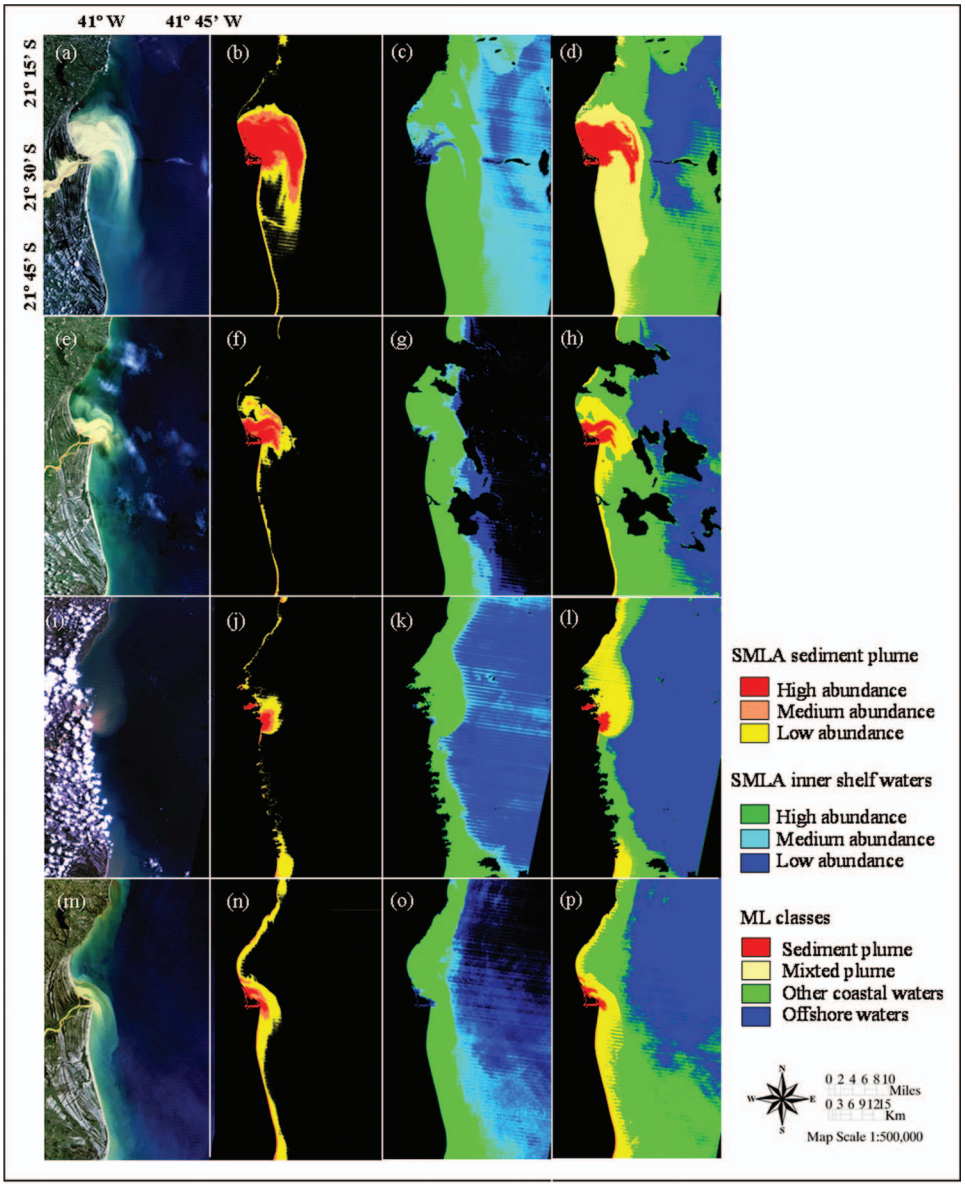

Fig. 4 True color composite (321) (a); SLMA classified sediment plume fraction (b); SLMA classified inner shelf water fraction (c); and ML classification (d), of the 1985 TM image. Same sequence for the 1986 image [(e)–(h)]; 1991 [(i)–(l)]; and 1994 image [(m)–(p)]. SMLA classes: High abundance: 0.66 to 1.00; medium 0.33 to 0.66; and low: 0.10 to 0.33.

summer seasons. Highlighted values correspond to the months of the available images with greatest river discharge (Fig. 7).

One can observe a slight tendency of decrease in the river discharge during this period (Fig. 7). Marengo and Alves[8] analyzed a longer time series of the PSR discharge along all the catchment area, from 1920 to 2004. They detected a significant decrease of the river discharge in many points, especially after 1955, which was not correlated to the rainfall regime or possible climate changes. The authors discussed that the observed changes in the PSR hydrologic regime were strongly related to anthropogenic activities, especially due to hydroelectric reservoirs constructed along the river, and the industrial and agriculture demand. In the present study we also analyzed some pluviometric data at the same station of the river discharge (not

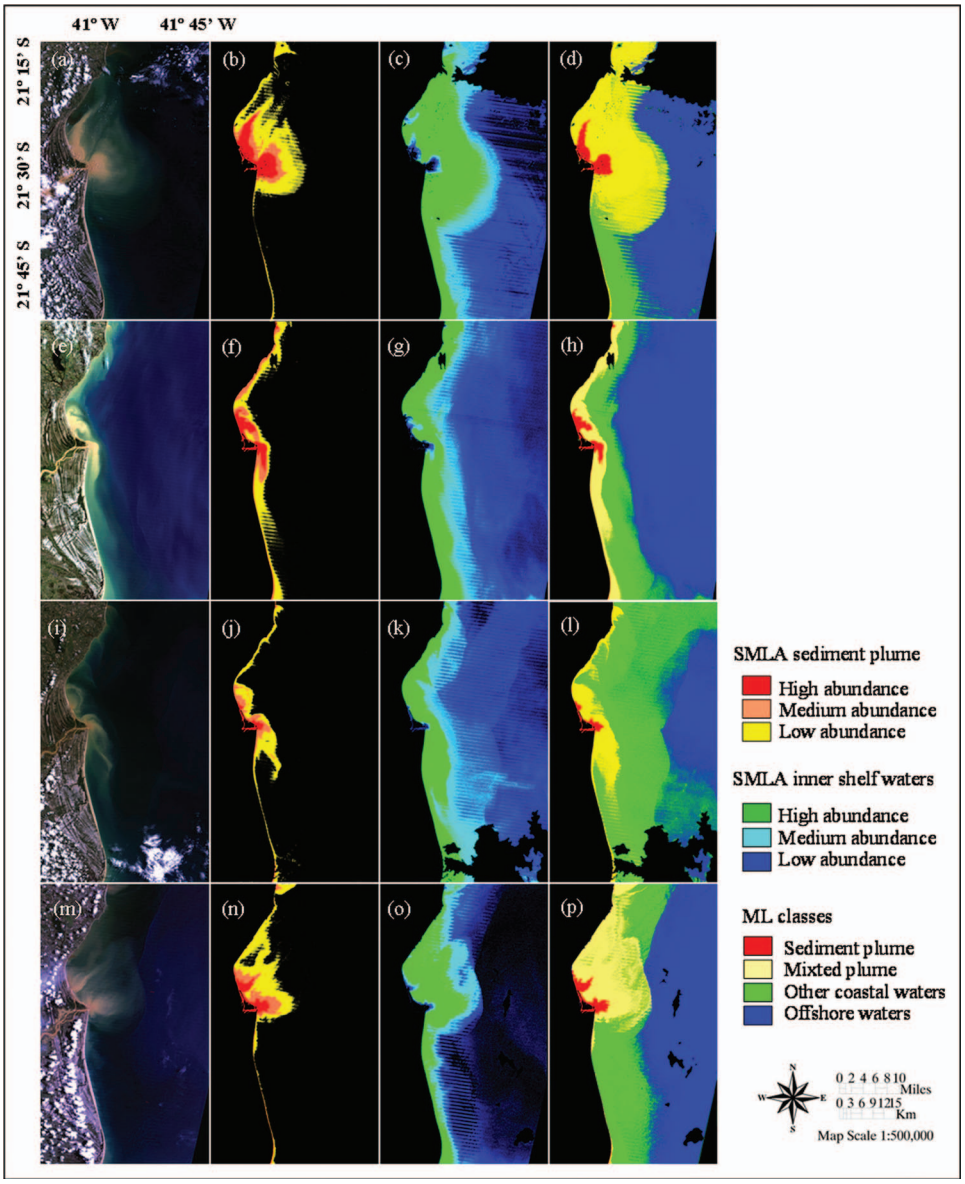

Fig. 5 True color composite (321) (a); SLMA classified sediment plume fraction (b); SLMA classified inner shelf water fraction (c); and ML classification (d), of the 1997 TM image. Same sequence for the 1999 image [(e)–(h)]; 2004 [(i)–(l)]; and 2005 image [(m)–(p)]. SMLA classes: High abundance: 0.66 to 1.00; medium 0.33 to 0.66; and low: 0.10 to 0.33.

shown), and no tendency was detected. This may be an indicative confirming the previous study, that indeed there could be a decreasing trend in the PSR discharge, which may be more related to land use changes rather than rainfall regimes or climate changes.

The river sediment plume area, mapped by both methods, had a high correlation with the river discharge: 0.95 ($p < 0.05$) for the ML and 0.94 ($p < 0.05$) for the SLMA. The correlation in between the two methods was of 0.95 ($p < 0.05$), confirming the high coherency between the classifications. Figure 8 shows how the sediment plume area, of the two classifications, varied closely with the river discharge.

There can also be observed a negative tendency of the river sediment plume through the period analyzed (Fig. 8). The greatest mapped plume area was in 1985 with 183 km^2. The river

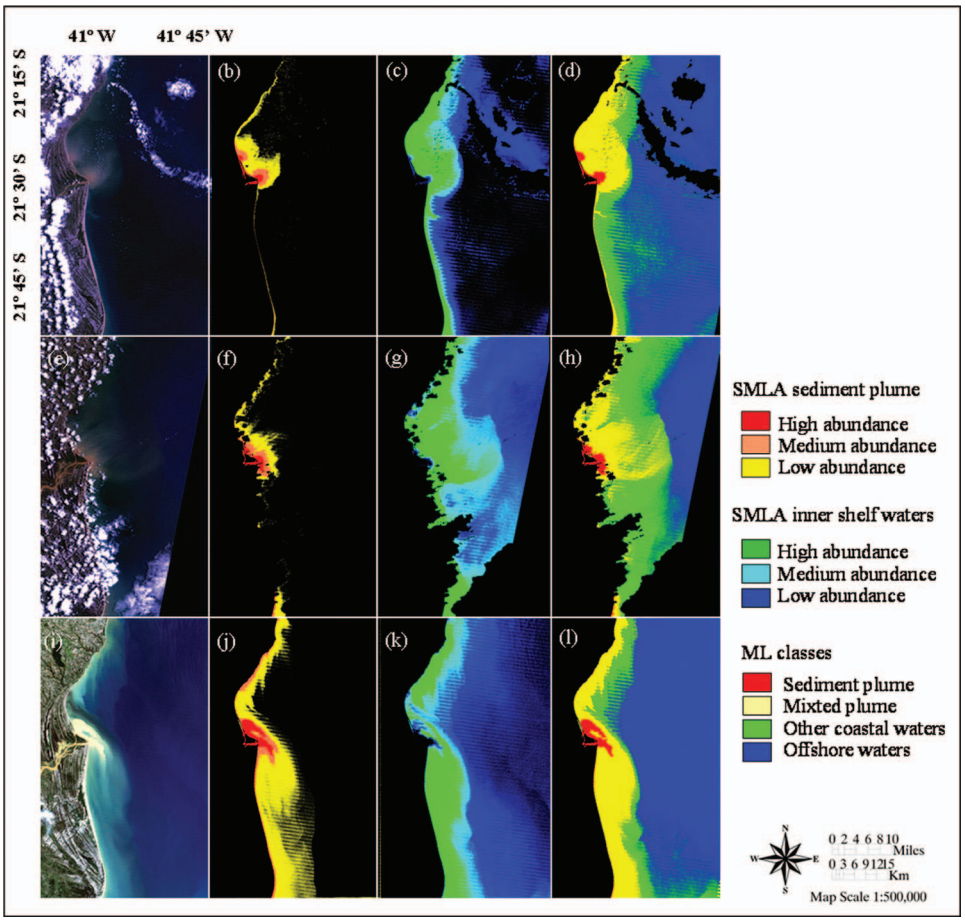

Fig. 6 True color composite (321) (a); SLMA classified sediment plume fraction (b); SLMA classified inner shelf water fraction (c); and ML classification (d), of the 2006 TM image. Same sequence for the 2007 image [(e)–(h)]; and 2009 [(i)–(l)]; SMLA classes: High abundance: 0.66 to 1.00; medium 0.33 to 0.66; and low: 0.10 to 0.33.

discharge in this date was of 2610 m^3 s^{-1} and the plume reached 14.1 km from the river mouth in the north-east direction (measured in the image). The smallest plume area was in 2006, with 15.7 km^2, with 864 m^3 s^{-1} of discharge and a maximum distance of 4.3 km achieved by the plume in the northeast direction.

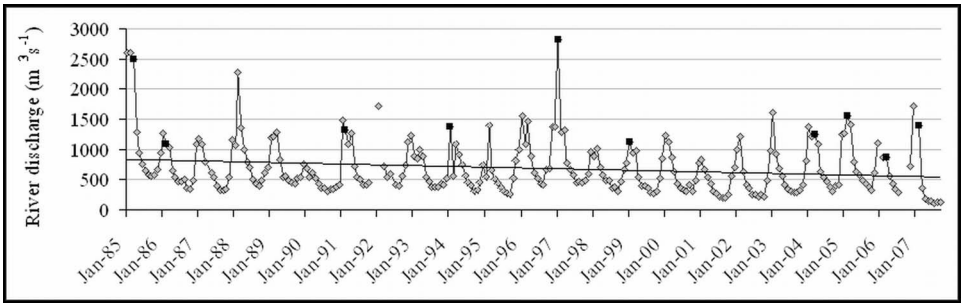

Fig. 7 River discharge from 1985 to 2008 at Campos (Rio de Janeiro, Brazil) station, with mean monthly values. Highlighted dots show the months of the acquired Landsat 5 images.

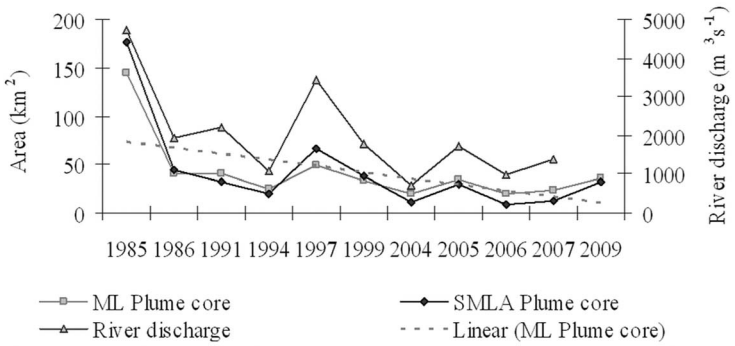

Fig. 8 River discharge values on the same date of the images acquired; area of the river sediment plume classified by the SLMA and the ML; and linear tendency of the SLMA plume area.

Lorenzzetti et al.[41] also investigated possible decreases of the sediment supply carried out by the São Francisco River plume, in northeast Brazil, with Landsat TM images, and found indicatives of a decrease in the sediment supply. They discussed causes related to the presence of hydroelectric reservoirs, which are known to retain the sediments along the river course. The PSR catchment area has several dam constructions which may have an important role in the impacts observed of the diminishing PSR discharge and sediment plume. Many worldwide researches have shown such impacts, and even others, related to the presence of dams in the river catchment area.[5,6,10,42] The loss of river discharge and sediment supply can cause much damage to the coastal environment, such as lower biological productivity, coastal erosion, and intrusion of salty water to the estuaries.[1]

Another important aspect to be considered on the dynamic equilibrium of the coastal region is the presence of mangrove ecosystems. Mangroves have been identified in literature as key ecosystems for sediment retention and other types of environmental services such as biogeochemical barriers for some pollutants (e.g., metals) and providers of habitat and organic matter for the coastal food chain. Notwithstanding, the mangrove located in the estuarine portion of the PSR has suffered great changes, with a loss of 20% of the mangrove vegetation from 1976 to 2001, i.e., a deforestation rate of approximately 7.5 $ha \cdot y^{-1}$ (Ref. 43). One of the causes of this deforestation pointed out by Bernini et al.[43] is the misbalanced sediment supply of the PSR due to dam construction, sand exploitation, and others. Changes in the sediment supply have caused higher variability in the PSR estuary coastline, with accumulation and erosion processes that disrupts the settlement of mangrove trees. The possible decrease tendency in the sediment plume shown in the present work may corroborate to the previous studies that already show effects of this decrease on the mangrove ecosystems.

The river plume not only carries out suspended inorganic sediments to the coast, but also nutrients and organic loads. These too have important roles in the coastal ecosystem, and may affect a much larger area, as they have lower sinking rates and can travel much farther from the river sediment plume boundary.[1] Souza et al. [22] studied the distance that the PSR plume can achieve offshore, by radioactive tracers. They encountered a distance of the river influence up to 32 km from the coast in the east direction during the rainy season. The approach determined diffusion coefficients of $\sim 30\ km^2 \cdot d^{-1}$ during the dry season (August, 2007) and $67\ km^2 \cdot d^{-1}$ for the wet season (March, 2008). The river plume can reach 16 km in 10 days during the dry period, while during the wet season reaches that same distance in 6 days at a speed ranging from 1.6 to $2.6\ km \cdot d^{-1}$. The instantaneous flux at this time of the year was $330\ m^3 \cdot s^{-1}$ and $780\ m^3 \cdot s^{-1}$, for dry and wet seasons, respectively. The greatest distance that the sediment plume achieved, measured by satellite in the present study, was of 14 km in the year of greatest discharge (1985). The influence of the PSR in the coast may therefore be much beyond the sediment plume boundary, and achieve a much greater area for other parameters, such as the phytoplankton distribution. In this manner, we analyzed the correlation between a phytoplankton dominated

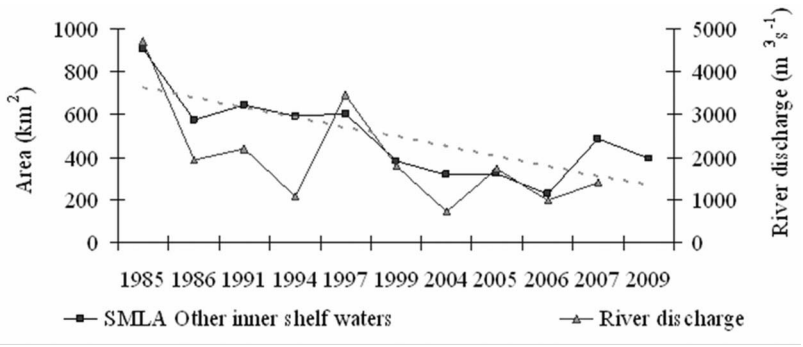

Fig. 9 River discharge values on the image acquisition dates; total area of the high abundance inner shelf waters, mapped by the SLMA, and linear tendency of the class.

inner shelf water class, derived from SMLA, and the river discharge, in order to evaluate the river influence on the coastal phytoplankton biomass. The correlation coefficient was 0.80 ($p < 0.05$), which is very high for a medium size river. The inner shelf water class also showed a negative tendency over the years (Fig. 9), indicating a possible decay of the river influence to the coastal phytoplankton biomass, due to the lower discharge.

The observations presented here certainly need more investigations with ground truth data to confirm the possible hypotheses. However, they reinforce earlier studies denoting a decrease of the PSR discharge due to land use changes over the past decades, and point out some possible effects in the PSR estuary, with a decrease of the river sediment plume and coastal phytoplankton biomass.

4 Final Considerations

Image classification techniques have been widely applied for land use mapping, but much less for aquatic systems. In this work, two methods used for this last proposal were compared in a tropical estuary: the ML and SLMA. Both classifications showed good results within primarily analysis. The SLMA, though, showed some advantages with more information of the spectral variability and distribution of the water constituents. This is very relevant for the analysis of river plume dispersion and areas of transition between water types.[19] Another advantage of the SLMA is that once the spectral library of the end-members is constructed, the classification is easily applied for all the time-series using only one standard reference. With the ML method, the training polygons had to be relocated on each image due to spatiotemporal variations in the water surface reflectance and cloud interference. This procedure is more time consuming and may carry some uncertainties in the spectral variations analyzed. One can argue that the water constituents may vary in their quality, and this way, different spectral references must also be used for spatiotemporal analysis.[17] This is true for a more detailed analysis of variations in the water quality. However, to analyze general changes, a fixed standard reference for each OAS may be considered more adequate, when spectral variations are not so high.

For future studies, the mapped fractions of the SLMA may also be associated with *in situ* measurements of the OAS, providing empirical models to estimate OAS's concentrations. The SLMA method should be applied with care as there are also some uncertainties associated with the assumptions that are not truly found in natural environments. Nonlinear relations of the spectral behavior between the OAS and difficulties in extracting pure elements from an image scene are still challenges in the SLMA, especially for optically complex waters.[21] More investigations of adequate procedures to obtain standard spectrums and to diminish spectral nonlinearity effects are required for this analysis.

Both the river sediment plume and phytoplankton dominated inner shelf waters had a coherency oscillation with the PSR discharge, and demonstrated a decrease tendency in the period

analyzed of 1985 to 2009. These are important indicatives of temporal changes in the hydrologic regime and water quality of the PSR estuary and coastal area, with decrease of the sediment supply and phytoplankton dominated waters, as a consequence of the lower outflow. Such effects may be related to land use changes in the PSR catchment area, especially with the presence of hydroelectric reservoirs.

The present work contributes with analysis of spectral mapping methods applied to the surface waters of the PSR estuary and coastal waters. The methods of relatively simple application were efficient to map the water types and demonstrate the spatial-temporal trend of the system, showing important indicatives of possible changes through the period analyzed. Further works concern *in situ* validation of the classifications, bio-optical modeling of the water components, and more research on environmental and anthropogenic changes in the PSR. These studies should collaborate with management adaptive strategies for the sustainable use of the PSR. The method presented in this work may also be applied for other small and medium size rivers along the Brazilian coast, to study their temporal evolution and contribution to the coastal and oceanic adjacent systems. The contribution of these rivers has been systematically neglected by researches on regional and global biogeochemical cycles, but they do have an important role that should be considered. The delineation of the river plumes along the Brazilian coast, and quantification of their inputs to the adjacent continental shelf, may be an important step to understand their relative importance for the Southwest Atlantic Ocean.

Acknowledgments

The author thanks INPE for providing level 2 preprocessed Landsat 5 images and ANA for river discharge data, both freely available online. Special thanks are also given to Dr. Leila Fonseca for preliminary orientations in the image processing. N.M.R has a PhD fellowship from the *Coordenação de Aperfeiçoamento de Pessoal de Nível Superior* (CAPES). We also thank the anonymous reviewers for their valuable comments that improved a lot of our work.

References

1. R. W. G. Carter, *Coastal Environments: An Introduction to Physical, Ecological and Cultural Systems of Coastlines*, 1st Edition (1990), 8th Ed. (2001), Academic Press, An Imprint of Elsevier Science, London, UK.
2. P. W. French, *Coastal Defenses: Processes, Problems and Solutions*, 384 p., Taylor & Francis, London (2001).
3. X. Ma, J. Xu, and M. Van Noordwijk, "Sensitivity of streamflow from a Himalayan catchment to plausible changes in land cover and climate," *Hydrolog. Process.* **24**, 1379–1390 (2010).
4. N. N. Rabalais, R. E. Turner, R. J. Díaz, and D. Justić, "Global change and eutrophication of coastal waters," *ICES J. Marine Sci.* **66**, 1528–1537 (2009).
5. W. L. Graf, "Dam nation: A geographic census of American dams and their large-scale hydrologic impacts," *Water Resour. Research* **35**(4), 1305–1311 (1999).
6. J. P. M. Syvitski, J. C. Vörösmarty, A. J. Kettner, and P. Green, "Impact of humans on the flux of terrestrial sediment to the global coastal ocean," *Science* **308**, 376–380 (2005).
7. ANA–Brazilian National Water Agency, "Região Hidrográfica Atlântico Sudeste" (Atlantic Southeast Hydrographical Region). Accessed on May 2010: http://www2.ana.gov.br/Paginas/portais/bacias/Atlanticosudeste (2010).
8. J. A. Marengo and L. M. Alves, "Tendências Hidrológicas da Bacia do Rio Paraíba do Sul. Revista Brasileira de Meteorologia," (Hydrological tendencies of the Paraíba do Sul River Basin), *Braz. J. Meteorol.* **20**(2), 215–226 (2005).
9. A. M. Duda and M. T. El-Ashry, "Addressing the global water and environment crises through integrated approaches to the management of land, water and ecological resources," *Water Int.* **25**(1), 115–126 (2002).

10. S. Apitz and S. White, "A conceptual framework for river-basin-scale sediment management," *J. Soils Sediments* **3**(3), 132–138 (2003).
11. P. Lavery, A. Wyllie, and P. Hick, "Water quality monitoring in estuarine waters using the Landsat thematic mapper," *Remote Sens. Environ.* **46**(3), 268–280 (1993).
12. Y. Wang, H. Xia, J. Fu, and G. Sheng, "Water quality change in reservoirs of Shenzhen, China: Detection using LANDSAT TM data," *Sci. Total Environ.* **328**, 195–206 (2004).
13. S. R. Phinn, A. G. Dekker, V. E. Brando, and C. M. Roelfsema, "Mapping water quality and substrate cover in optically complex coastal and reef waters: An integrated approach," *Mar. Pollution Bull.* **51**, 459–469 (2005).
14. Y. Oyama, B. Matsushita, T. Fukushima, J. Chen, T. Nagai, and A. Imai, "Testing the spectral decomposition algorithm (SDA) for different phytoplankton species by a simulation based on tank experiments," *Int. J. Remote Sens.* **31**(6), 1605–1623 (2010).
15. E. J. D'sa and R. L. Miller, "Bio-optical properties of coastal waters," in *Remote Sensing and Digital Image Processing, Series: Remote Sensing of Coastal Aquatic Environments*, R. L. Miller, C. E. D. Castillo, and B. A. Mchee, Eds., Vol. 7, pp. 129–155 (2005).
16. A. C. Thomas and R. A. Weatherbee, "Satellite-measured temporal variability of the Columbia River plume," *Remote Sens. Environ.* **100**, 167–178 (2006).
17. T. Lihan, S. Saitoh, T. Iida, T. Hirawake, and K. Iiad, "Satellite-measured temporal and spatial variability of the Tokachi River plume," *Estuarine Coastal Shelf Sci.* **78**, 237–249 (2008).
18. E. M. Novo and Y. E. Shimabukuro, "Spectral mixture analysis of inland tropical waters," *Int. J. Remote Sens.* **15**(6), 1351–1356 (1994).
19. A. J. Warrick, L. A. K. Mertes, L. Washburn, and D. A. Siegel, "Dispersal forcing of southern California river plumes, based on field and remote sensing observations," *Geosci. Marine Lett.* **24**, 46–52 (2004).
20. C. M. Rudorff, E. M. Novo, and L. S. Galvão, "Spectral mixture analysis of inland tropical Amazon floodplain waters using EO-1 hyperion," *IEEE Trans. Geosci. Remote Sens.* 128–133 (2006).
21. C. M. Rudorff, L. S. Galvão, and E. M. Novo, "Reflectance of floodplain waterbodies using EO-1 Hyperion data from high and receding flood periods of the Amazon River," *Int. J. Remote Sens.* **30**(10), 2713–2720 (2009).
22. T. A. Souza, J. M. Godoy, M. L. D. P Godoy, I. Moreira, Z. L. Carvalho, M. S. Salomão, and C. E. Rezende, "Use of multitracers for the study of water mixing in the Paraíba do Sul River estuary," *J. Environ. Radioact.* **101**, 564–570 (2010).
23. G. Chander, B. L. Markham, and D. L. Helder, "Summary of current radiometric calibration coefficients for Landsat MSS, TM, ETM+, and EO-1 ALI sensors," *Remote Sens. Environ.* **113**, 893–903 (2009).
24. IOCCG, "Atmospheric correction for remotely-sensed ocean-colour products," M. Wang, Ed., *Reports of the International Ocean-Colour Coordinating Group, no. 10, IOCCG*, Dartmouth, Canada (2010).
25. IOCCG, "Remote sensing of ocean colour in coastal, and other optically-complex, waters," S. Sathyendranath, Ed., *Reports of the International Ocean-Colour Coordinating Group, no. 3, IOCCG*, Dartmouth, Canada (2000).
26. D. A. Siegel, M. Wang, S. Maritorena, and W. Robinson, "Atmospheric correction of satellite ocean color imagery: The black pixel assumption," *Appl. Opt.* **39**, 3582–3591 (2000).
27. M. Wang, S. Son, and W. Shi, "Evaluation of MODIS SWIR and NIR-SWIR atmospheric correction algorithms using SeaBASS data," *Remote Sens. Environ.* **113**, 635–644 (2009).
28. E. F. Vermote, D. Tanre,, J. L. Deuzé, M. Herman, and J. J. Morcrette, "Second simulation of the satellite signal in the solar spectrum, 6S: An overview," *IEEE Trans. Geosci. Remote Sens.* **35**(3), 675–686 (1997).

29. D. G. Hadjimitsis, C. Clayton, and L. Toulios, "Retrieving visibility values using satellite remote sensing data," *Phys. Chem. Earth, Parts A/B/C* **35**(1-2), 121–124 (2010).
30. F. S. C. Oliveira, M. Kampel, and S. Amaral, "Multitemporal assessment of the geomorphologic evolution of the Restinga of Marambaia, Rio de Janeiro, Brazil," *Int. J. Remote Sens.* **29**(19), 5585–5594 (2008).
31. A. J. Richard, *Remote Sensing Digital Image Analysis*, p. 340, Springer-Verlag, New York (1993).
32. R. Congalton and K. Green, *Assessing Accuracy of Remotely Sensed Data: Principles and Practices*, 137 p., CRC/Lewis Press, Boca Raton, Florida (1999).
33. J. B. Adams, M. O. Smith, and P. E. Johnson, "Spectral mixture modeling: A new analysis of rock and soil types at the Viking Lander 1 site," *J. Geophys. Res.* **91**, 8098–8112 (1986).
34. A. Green, M. Berman, B. Switzer, and M. D. Craig, "A transformation for ordering multispectral data in terms of image quality with implications for noise removal," *IEEE Trans. Geosci. Remote Sens.* **26**(1), 65–74 (1988).
35. F. A. Kruse, A. B. Lefkoff, J. W. Boardman, K. B Heidebrecht, A. T. Shapiro, P. J. Barloon, and A. F. H. Goetz, "The spectral image-processing system (Sips)—interactive visualization and analysis of imaging spectrometer data," *Remote Sens. Environ.* **44**(2–3), 145–163 (1993).
36. M. P. Otero and D. A. Siegel, "Spatial and temporal characteristics of sediment plumes and phytoplankton blooms in the Santa Barbara Channel," *Deep-Sea Res., Part II* **51**(10-11), 1129–1149 (2004).
37. J. G. Lyon, K. W. Bedford, C. C. J. Yen, D. H. Lee, and D. J. Mark, "Determination of suspended sediment concentrations from multiple day Landsat and AVHRR data," *Remote Sens. Environ.* **25**, 107–115 (1988).
38. M. A. Lodhi, D. C. Rundquist, L. Han, and M. S. Kuzila, "Estimation of suspended sediment concentration in water using integrated surface reflectance," *Geocarto Int.* **13**(2), 11–15 (1998).
39. J. M. Froidefond, L. Gardel, D. Guiral, M. Parra, and J. F. Ternon, "Spectral remote sensing reflectance of coastal waters in French Guiana under the Amazon influence," *Remote Sens. Environ.* **80**, 225–232 (2002).
40. D. A. Toole, D. A. Siegel, D. W. Menzies, M. J. Neumann, and R. C. Smith, "Remote-sensing reflectance determinations in the coastal ocean environment: Impact of instrumental characteristics and environmental variability," *Appl. Opt.* **39**(3), 456–469 (2000).
41. J. A. Lorenzzetti, E. Negri, B. Knopers, and P. R. P. Medeiros, "Uso de imagens LANDSAT como subsídio ao estudo da dispersão de sedimentos na região da foz do rio São Francisco," (Use of Landsat images as subsidies for the study of sediment dispersion at the estuary region of São Franscisco River), *Brazilian Symposium of Remote Sensing*, Brazil, pp. 3429–3436 (2007).
42. J. A. Marengo, J. Tomasella, and C. R. Uvo, "Trends in streamflow and rainfall in tropical South America: Amazonia, eastern Brazil, and northwestern Peru," *J. Geophys. Res.* **103**(D2), 1775–1783 (1998).
43. E. Bernini, R. Ferrreira, L. F. Carvalho e Silva, A. P. Mazurec, M. T. Nascimento, and C. E. Resende, "Alterações na cobertura vegetal do manguezal do estuário do rio Paraíba do Sul no período de 1976 a 2001," (Changes in the forest coverage of the mangrove of the Paraíba do Sul river estuary during the period of 1976 to 2001), *Revista da Gestão Costeira Integrada* (2010) (in press, www.aprh.pt/rgci).

Biographies and photographs of the authors not available.